Materials Innovations

HEXA Publishers

Perovskite Materials | Review Article | http://doi.org/10.54738/MI.2022.21101

Computational Perspective on Physical Aspects of Anti-perovskite Compounds Using ab-initio Study

Nazia Erum[1]*

1 Institute of Physics, Bahauddin Zakariya Univeristy, Multan, Pakistan

Received: 002 September 2022

Accepted: 11 November 2022

Published: 28 November 2022

Citation: Erum N (**2022**) Computational Perspective on Physical Aspects of Anti-perovskite Compounds Using ab-initio Study. *Materials Innovations 2* (11), 298-316.

***Correspondence**: (Nazia Erum)
email:erum.n@hotmail.com

Published By Hexa Publishers

ISSN
Electronic: 2790-1963

ABX_3 perovskites, the biggest family of crystalline materials, have received enormous research attention on a global scale, mainly due to their extensive multifunctionality and the fascinating scientific principles that underlie them. While, anti-perovskites (X_3BA), are technically inverted perovskite derivatives, they are a significant family of useful materials. Anti-perovskites display a wide range of unusual physical and chemical properties, inheriting the adaptable structural characteristics of perovskites while being rich in cations at X sites. These compounds received less attention, thus systematic assessment is urgently required to widespread its applications. This article summarizes recent developments in innovative anti-perovskite materials application and their properties, including, superconductivity magnetic, electric, elastic, and optical properties. In this critical review, we first overview the reported compositions, structural stabilities, and ionic conductivities of anti-perovskites. We then discuss the different properties related to Anti-perovskites. We close by reviewing the use of anti-perovskites Lithium ion batteries and suggest some practices for the community to consider.

Keywords: Computational, ab-initio, Anti-perovskite

INTRODUCTION

Perovskites are substances with the general formula ABX_3, a basic structure with built-in potential for structural complexity and surprising features. Perovskites name was assigned in 1839 after the Russian mineralogist L. A. Perovski[64]. The classic example of an ABX_3 perovskite is $CaTiO_3$, which was initially found in the Ural Mountains of Russia. The A and B sites are occupied by cations while the X site is an anion.[15]. Perovskites retain a vital role in solid-state chemistry and physics. Due to their multiple important features that help the modern world function, including magnetism, ferroelectricity, multiferroicity, superconductivity, and the capacity to serve as catalysts and battery materials[59].

Anti-perovskites or inverse perovskites are inorganic compounds with a perovskite structure but structurally inverted X_3AB[49]. In which the cation and anion sublattices are reversed, resulting in anions occupying the A and B sites while cations are present at the X site. The A-site anions are cub-octahedrally coordinated to 12 nearest-neighbor cations, while the B-site anions are octahedrally coordinated to six cations. Corner-sharing BX_6 octahedra make up the structure's 3D skeleton. The optimal anti-

perovskite structure is cubic, depending on temperature, pressure, and material composition. However, it consists of tetragonal, orthorhombic, rhombohedral, and hexagonal phases as well[49]. The abundant X site cations give anti-perovskites unusual physical and chemical features related to d-spin states or ion transport. Small anions are typically found at the B site, while monovalent or divalent cations are typically found at the X site[45].

Anti-perovskite compounds are crucial substances because they provide intriguing and worthwhile physical characteristics that perovskite substances don't have. They have demonstrated a number of intriguing qualities, including magnetism, ionic conductivity, superconductivity, negative thermal expansion, the capacity to serve as photoluminescence host materials, among others. It is quite probable that this exciting research will spark a new phase in the creation of functional anti-perovskites. They have attained lot of attention for their excellent results across variety of fields, particularly in energy storage batteries. To improve the energy issue, anti-perovskites offer huge potential because they have good thermoelectric (TE) features. Waste heat is immediately transformed to electrical energy in thermoelectric systems. To attain great efficiency, researchers are looking for appropriate materials for thermoelectric generators. Band gaps in good thermoelectric materials are often both large enough to have a large See beck coefficient and tiny enough to have an electrical conductivity. The family of anti-perovskite materials includes all different types of compounds, including metals, semiconductors, insulators, and superconductors, making them useful in a wide range of applications. Solids with enhanced ionic conductivity are preferred in batteries over organic liquid electrolytes[47] .

The anti-perovskites exhibit unusual valence states and a mixture of ionic, covalent, and metallic bonds. However, due to oxygen's high ionicity and tendency to form ionic bonds with the opposing cationic A and B elements, oxide anti-perovskites (A_3BO) are hardly stable in ambient conditions. For s-block and transition-metal based anti-perovskites, this restriction might be eliminated where additional covalent and metallic bonds are necessary for their crystallographic stability. When combined with different elemental groups of d-block transition metals and p-block post-transition metals to create a crystal, f-block lanthanides can be included in the boundary for such stable anti-perovskite compounds. Because of the numerous bonding characteristics with enhanced covalency and/or metallicity, such compounds may display a variety of electrical properties. In addition, because f-electrons frequently contribute to strongly correlated electronic properties, it is possible to expect a variety of unusual quantum phenomena in f-block anti-perovskites, which can display unusual electronic band structures resulting from the mixed chemical bonds. The existence of thermodynamically stable anti-perovskites based on f-block elements and their new features are currently under investigation[36].

Anti-perovskites benefit from both their cation-rich properties as well as the inherent potential of the perovskite-type structure. Due to the flexibility of their structure, anti-perovskites are relatively easy to make, which allows for a variety of chemistries. Further research is carried out to broaden the scope structural and functional views that significantly advance the solid-state physics[16]

An anti-perovskite solid state electrolyte is thought to transport ions primarily through the movement of defects. In order to have an impact on the design of future materials as a solid-state electrolyte, it is important to understand how different types of defects, such as interstitials and alkali ion vacancies, move differently in lithium-based anti-perovskites. For X-ray photon correlation spectroscopy (XPCS) measurements, a single crystal would be required. It is recommended to investigate XPCS because it would provide information on structural changes across the crystal on a time scale similar to that of defects moving through the lattice. This has been carried out on different electrolytes to understand ions.[64]

There is a knowledge gap regarding how effectively materials with this structure can be utilized and how these properties are affected by the symmetry and distribution of defects in these materials. Anti-perovskites' tracking of these characteristics in relation to non-Arrhenius ionic conduction behavior has not been thoroughly investigated to offer a theoretical and scientific basis for further design of these materials.[64] The number of anti-perovskite compounds is still very limited compared with the great possibilities shown in the elemental periodic table. Comparing the small number of anti-perovskite compounds to the many possibilities shown by the elemental periodic table. Due to lack of quantitatively discovered anti-perovskites, studies on anti-perovskites are still uncommon, with only fifty publications published annually. In some cases, the recently found anti-perovskites are simply treated as intermetallic compounds or dual-metal nitrides/carbides without being aware of their special structure because the name "anti" is not commonly accepted. The significance of anti-perovskites, however, considerably exceeds our expectations[45].

BACKGROUND

Anti-perovskites, also known as Inverse perovskites, have a rich history and have been used in numerous technological applications due to their distinctive and varied properties, which are brought about by their adaptable and customizable structure. It was first suggested that the anti-perovskites has been used as energy storage materials

after their discovery in 1915. Numerous anti-perovskite materials have been composed and studied so far. Na_3NO_3 was the first Na-rich anti-perovskite to be reported, by Zintl and Morawietz in 1938[12].

Numerous studies on the various physical characteristics of manganese-based anti-perovskites materials with the general formula $AXMn_3$ have been conducted since the 1960s (A is a metal or semiconducting elements and X is C or N)[30]. Researchers from all around the world have been particularly interested in the discovery of superconductivity in $MgCNi_3$[31]. Hartwig et al. reported the initial structural conductivity analyses of Li-rich anti-perovskites ($Li_2(OH)Br$ and $Li_2(OH)Cl$) in 1981.[72] Using impedance testing, 1H and 7Li NMR spectroscopy, and ionic conductivity measurements, Schwering et al. in 2003 fully investigated the ionic conductivity and phase transition of Li_3-n(OHn)X (0.83 n $_2$; X = Cl, Br)[71 28]. In 2004, Gabler et al manufactured a new class of anti-perovskites $SbNX_3$ and $BiNX_3$ (X = Sr and Ba) and reported diamagnetic semiconducting nature[22]. These anti-perovskites also have been suggested to be useful in the thermal power generation processes[31]. In 2010, Hichour et al explored the pressure dependent properties of $ANSr_3$ (A = As, Sb and Bi) anti-perovskites by using Engel–Vosko generalized gradient approximation.[17]

Recently, inverse hexagonal perovskite structures ($Sr_{3-x}Ba_xN$) E (E = Sb, Bi) based on anion-centered [N_3A_6] octahedra (A = Sr, Ba) were reported by Gaebler and Niewa (2007). These structures correspond to the 2H, 4H, and 9R polytypes. The x compositional parameter regulates the probability of a specific polytype occurring[49]. Hichour et al. (2010) investigated the pressure dependent properties of $ANSr_3$ (A = As, Sb, and Bi) anti-perovskites using the Engel-Vosko generalized gradient approximation and found a mixture of covalent and ionic nature, while the small direct band gap they found suggested suitable optical applications.[17]

Li_3OX (X = Cl or Br) with an ionic conductivity more than 10^{-3} S cm^{-1} at room temperature was reported by Zhao et al. in 2012.[38] LiCl + 2LiOH = Li_3OCl + H_2O was created by heating molten LiX and LiOH as the initial materials under vacuum for several days. $Li_{3-2x}Ba_xOCl$ glass (x = 0.005) was reported by Braga et al. in 2014 to have an unusually high ionic conductivity of 2.5 10-2 S cm^{-1} at 25 °C. (2) The stated synthesis must be acknowledged as being ambiguous. LiOH, LiCl, and $Ba(OH)_2$ were heated in a Teflon reactor with a few drops of water at 220-240 °C to create the electrolyte[28].

In 2015, Wang et al. reported various aspects of Na_3OX (X = Cl, Br, I). Both Na_3OCl and Na_3OBr are cubic structures at room temperature. Na_3OBr shows a higher ionic conductivity compared to Na_3OCl, though the activation energy of Na_3OBr (0.76 eV) is higher than that of Na_3OCl (0.63 eV)[37] . In 2016, researchers of the same group conducted follow-up research and systematically examined the reaction in the Li_3OX production mechanism. In contrast to Li_2O and LiCl, their theoretical analysis revealed that Li_3OCl is not thermodynamically stable[14].

Sun et al. created Na_3OBH_4 from Na_2O and $NaBH_4$ for the first time in 2019. The reported ionic conductivity, which is many orders of magnitude greater than Na_3OX (X = Cl, Br, and I), is 4.4 10^{-3} S cm-1 at room temperature. Interest in anti-perovskite materials has increased significantly due to recent discovery of their potential as Li- and Na-based solid electrolytes for solid-state batteries. The work of Zhao and Daemen in 2012, which first revealed superionic conductivity in the Li-rich anti-perovskites Li_3OCl, Li_3OBr, and $Li_3OCl_{0.5}Br_{0.5}$, was largely responsible for this increase in interest[8]. The first anti-perovskite oxides were discovered accidently when trying to make Sr_3Sn, which was found to only be stable with the addition of oxygen, yielding Sr_3SnO[70].

PROPERTIES OF ANTI-PEROVSKITES

Anti-perovskites have been discovered to have a variety of interesting properties such as giant magnetoresistance, nearly zero temperature coefficient of resistivity, and, depending on their chemical composition, a wide range of physical properties ranging from semiconducting to magnetic and superconducting[19]. Over the past ten years, they have been extensively studied for their new features, and because of the wide range of band gaps they exhibit. They have attracted a lot of attention from researchers interested in using them for a variety of commercial applications. Small band gap anti-perovskites have become a possible candidate for a number of optical systems. As a result, anti-perovskites may resemble metals, nonmetals, semiconductors, and superconductors, as well as other fascinating material properties.[7]

A material's mechanical, thermoelectric, optical, magnetic, and other physical characteristics are significantly influenced by its electronic properties. Little changes in the electrical structure have a big impact on these qualities. Band structures and densities of states must be thoroughly understood in order to use materials in optical, memory storage, and thermoelectric devices[47]. The results of the initial principal band structure calculations have recently contributed significantly to our understanding of the coupling mechanism, electronic, structural, elastic, spectroscopic, chemical bonding, and phase stability of various superconducting materials. Additionally, some efforts were made to describe the electronic structure of the aforementioned anti-perovskites[48]. Spider plot of the anti-perovskite electrolyte materials is shown in Figure 1. For ionic conductivity, the three stellar anti-perovskites ($Li_3OCl_{0.5}Br_{0.5}$,

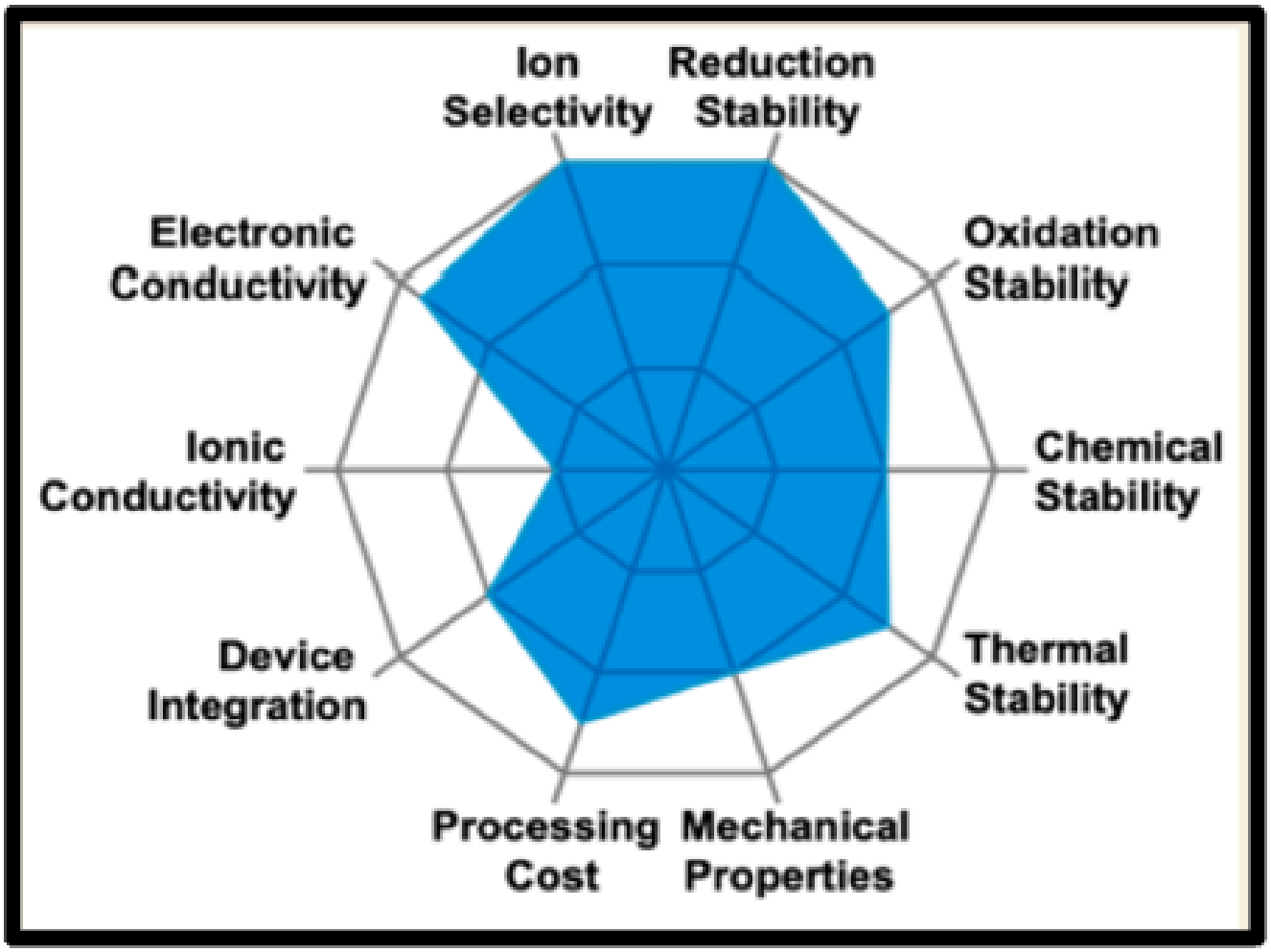

Figure 1. Spider plot of the anti-perovskite electrolyte materials.[60] Reproduced with permission from ref 20. Copyright 2017 Springer nature reviews.

Na_3OBH_4, and $Li_{3-2x}Ba_xOCl$ glass (x = 0.005)), which need further examination are not included. The value of each property for anti-perovskite electrolyte is estimated by comparing with reported oxide, sulfide, hydride, halide, thin films, and polymer solid electrolytes[48].

Structural properties of Anti-perovskites

Structural determination is an essential initial step in figuring out structure-property interactions; that is, the structure must be understood if structure-property relationships are to be effectively defined and characterized. Most anti-perovskite compounds are known to deviate from the ideal cubic structure, creating orthorhombic or tetragonal phases depending on temperature and pressure, similar to the perovskite structure with ABX_3 stoichiometry and cubic structure, where A is a larger monovalent or divalent cation (such as Na^{+1} , K^{+1} , Ca^{+2} , crystal Sr^{+2} , Ba^{+2}), positioned at the cubic corner sites, B is a smaller pentavalent or tetravalent transition-metal atom (such as Ti^{+4} , Nb^{+5} , Mn^{+4} , Zr^{+4}), positioned at the center of the cube, and X is an anion (non-metal, such as N^{-3} , O^{-2} , F^{-1} , Cl^{-1}), positioned at the center of the cube face. The cubic anti-perovskite type is a regular cubic perovskite with the chemical formula where the metal atoms have switched places with the non-metal atoms within the unit cell. The A metal atoms are positioned at the cube corner sites and the non-metal atoms are positioned at the body-centered positions in the structure AXM_3, where A is a major group (III-V) element. M is a transition (s-d) metal, and X is either carbon or nitrogen, in which the atoms are arranged in face-centered configurations[60].

The relative sizes of the ionic radii of a compound's constituent atoms as well as its chemical formula determine whether it will form an anti-perovskite structure. The Goldschmidt tolerance

factor, which is determined by the radii, r_A, r_B, and r_X, of the A, B, and X ions, is used to express this limitation. For perovskites, the tolerance factor (t) was developed to determine their probable structural symmetry and crystallographic stability. This is defined by the equation

$$t = (r_A + r_X)/ [(r_B + r_X)] \quad (1)$$

Here r_A, r_B, and r_X are the ionic radii of the corresponding ions. Lower t values yield tetragonal or orthorhombic structures or other structures with even lower crystallographic symmetry, and the cubic structure is likely to exist when t is in the range of 0.85-1.0. The equation $r_A + r_X = 2(r_B + r_X)$ can also be used to determine the relationship between the ionic radii in a cubic ionic anti-perovskite, X_3BA. Most anti-perovskites are composed of p-elements (such as Al, Ga, and Ge) that prefer covalent bonding and d- or f-elements (such as V, Cr, Mn, and Ni) that prefer metallic bonds. In such cases, it is impossible to use the tolerance factor to determine the existence of a postulated anti-perovskite or predict the crystallographic symmetry. Beznosikov attempted to anticipate metallic nitrides with an anti-perovskite structure by taking into account t, R_A/R_B, and the types of interatomic bonds[43]. However, the predictability and reliability of the method have yet to be proven. Even when the above-mentioned equation is not completely followed, the cubic structure is kept in metallic X_3BA compounds, departing from the ideal situation[45].

Although real compounds sometimes adopt pseudo cubic or lower symmetries, ideal anti-perovskites adopt a cubic geometry. Anti-perovskites exhibit structural distortions less frequently than perovskites, although structural distortions will undoubtedly affect their physical characteristics. Perovskite distortions can always be divided into a number of simple parts. a) the octahedra tilting, b) distortion of the octahedra, and c) displacement of the cations. The rigid octahedra's rotation creates a total of 23 possible space groups, and among them, tilting of the octahedra often dominates the overall crystal structure[29,58].

The unusual coordination environment of cation X (i.e., the X-X distance and linear two-fold coordination versus six-fold coordination in perovskites), which plays a critical role in magnetic interactions or the crystal field strength, is one of the most important structural features of an anti-perovskite. Another notable structural property of anti-perovskites is their X site richness. Magnetism and ionic conductivity, for example, are significantly related to the X-rich characteristic of anti-perovskites. The high-temperature superionic conductivity of $NaMgF_3$ and $(K,Na)MgF_3$ perovskites inspired the discovery of superionic conductivity in Li-rich anti-perovskites (LiRAPs)[38].

Lithium-rich Anti-perovskites (LiRAPs) with the generic formula Li_3OX (X = Cl, Br) are emerging as feasible solid electrolytes in all-solid-state lithium-ion batteries (LIBs)[14]. In order to potentially overcome both the safety issues with liquid electrolytes and the high interfacial resistance generally associated with solid electrolytes, Li_3OCl has also been considered as a "Quasi-solid-state electrolyte." A Li anode was covered with a 500 nm-thick Li_3OCl layer, which caused a notable decrease in its polarization and prevented the usual solvents present in liquid electrolytes from decomposing at 4.5 V. More recently, Li_2OHCl has been suggested as a coating material for various solid electrolytes. In situ Li_2OHCl-coated garnet solid electrolytes were prepared using a straightforward aqueous method by Lai et al., and it was successfully demonstrated that this method decreased the garnet's sintering temperature from 1200 to 350 °C while also improving its capacity to inhibit lithium dendrite growth. Li_2OHCl's structure at room temperature is still relatively elusive. Based on both experimental and/or computational studies, various structures and space groups have recently been suggested; all of these are compiled in the table[23,50].

Nitrides anti-perovskite X_3BN (X = Ca, Sr, Ba, Mn, Ni, Co; B is a group-IV or group-V element), In order to release excess nitrogen gas during high-temperature sintering, nitrogen-excess reagents may be used. This approach was used to synthesis a family of anti-perovskites Ca_3MN (M = P, As, Sb, Bi, Ge, Sn, Pb).[41]. Ca_3ZN (Z = As, Sb, Bi) calcium-based nitride compounds have a cubic anti-perovskite structure. According to other reports, Ca_3AsN exists in the orthorhombic phase as well. The structural properties of these cubic anti-perovskite materials were calculated using the Birch-Murnaghan equation of state, which was fitted to the unit cell volume versus unit cell energy.

A promising water oxidation electro catalyst was recently produced using an anti-perovskite-based hybrid with a porous conductive $Ni_3yCu_{1-x}N$ core and an amorphous FeNiCu (oxy) hydroxide shell[12]. The Cu-excess anti-perovskite Ni_3CuN+Cu was originally created from a mixture of Cu and Ni powders using solid-gas reactions for the construction process of the p-Ni3yCu1-xN/ FeNiCu hybrid. Excess Cu was included on purpose to act as a sacrifice template for the development of rich pores during the etching process that followed. After that, a Fe_{3+} aqueous solution was used to etch the polycrystalline material to create a FeNiCu (oxy)hydroxide colloid, which was then deposited on the surface of the anti-perovskite phase.

The $AXMn_3$ compounds behave like metals, possessing metallic conductivity, high thermal conductivity, and good mechanical properties, in contrast to their perovskite equivalents (i.e., $RMnO_3$). Additionally, the components used to create the anti-perovskite $AXMn_3$ compounds are cheap and non-toxic. These benefits make $AXMn_3$ potentially useful

in domains where metallic properties (such as high electrical or thermal conductivity, high rigidity, etc.) would be desired[30]. For the study of their fundamental physical properties, numerous thermodynamically stable anti-perovskites can be produced using conventional high-temperature synthetic techniques. Metastable anti-perovskites or those with a special stoichiometry can potentially be produced using low-temperature soft chemical techniques like ammonolysis.

Additionally, contemporary methods for creating nanosized materials can be extensively used in the production of anti-perovskites with substantially. Anti-perovskites appear to already make up nearly half of the periodic table's components. In actuality, the claimed anti-perovskites contain no more than ten components. In comparison to the vast possibilities shown in the elemental periodic table, the number of anti-perovskite compounds is still quite limited. Schematic illustrating the Li diffusion in anti-perovskites through the Cl−O−Cl triangular bottleneck is shown in Figure 2.

Optical properties of Anti-perovskites

Optical properties are taken from carefully computed band structures and can thus be considered precise for illustrating optical applications. The complex dielectric constant $\varepsilon(\omega) = \varepsilon_1(\omega) + i\varepsilon_2(\omega)$ is one of the most powerful parameters for elaborating a material's optical response to radiations. The actual dielectric constant $\varepsilon_1(\omega)$ represents scattering, while the imaginary dielectric constant $\varepsilon_2(\omega)$ represents absorption of incident radiations. The absorption can be calculated by adding all of the energy transitions from occupied to unoccupied states[7]. The $\varepsilon_1(\omega)$ can be deduced from $\varepsilon_2(\omega)$ by employing Kramer–Kroning relation[66]

$$\varepsilon_1(\omega) = 1 + p \qquad (2)$$

Refractive index, $n(\omega)$, shows the ability of a medium to allow the electromagnetic (EM) radiations to travel through it. Refractive index for anti-perovskites is calculated by using the following expression[57]. M Hassan et al calculated the refractive index n (0) for Ca_3PbO, Sr_3PbO and Ba_3PbO, which are 3.39, 3.40 and 4.08 and are in good accordance with the static values of the real dielectric constant, $\varepsilon_1(0)$, revealing the accuracy of the present computations[7]. Ca_3PbO has the smallest cubic lattice constant and is less stable due to the least amount of energy released, whereas Ba_3PbO has the largest lattice constant and is the most stable due to the most amount of energy released. The studied anti-perovskites have a narrow direct band gap, indicating that they could be used in optical and TE applications. Because of the cationic variation, the absorption reveals a red shift for tuning the optical properties within the visible and ultraviolet energy ranges.

Hichour et al. explored the pressure dependent properties of $ANSr_3$ (A = As, Sb and Bi) anti-perovskites by using Engel–Vosko generalized gradient approximation. He observed mixed covalent and ionic nature, while the observed narrow direct band gap suggested suitable optical applications[17]. The optical properties of X_3ZN (X = Ca, Sr, Ba; Z = As, Sb, Bi) anti-perovskite compounds, such as the dielectric function (real and imaginary parts), refractive indices n(x) and k(x), reflectivity R(x), and optical conductivity r(x), were computed using the TB-mBJ potential. In the UV region, they display high absorption peaks and optical conductivity. As a result, these compounds are extremely useful in high frequency optoelectronic devices. Maximum reflectivity is obtained in the negative area of the dielectric function's real portion[48].

Chi et al. presented the synthesis of $AsNMg_3$ and $SbNMg_3$. He applied semi empirical band structure calculation model to demonstrate that $AsNMg_3$ has an extremely wide energy gap (9.0 eV), implying that it is an insulator.[10] The electronic properties are briefly described in order to adequately interpret their optical aspects. For the determination of the equilibrium lattice constant and bulk modulus of each material, the total energy was calculated at different volumes. The bulk modulus, pressure derivative, and equilibrium lattice constant were calculated by fitting the energy versus volume curve to the Murnaghan equation of state. As shown by the electronic band structures of the two compounds, $AsNMg_3$ has an indirect band gap semiconductor, whereas $SbNMg_3$ has a direct band gap semiconductor. The GGA is used to calculate the optical properties at the equilibrium lattice constant. The inter band contribution to the imaginary part of the dielectric function that was obtained through the calculations is shown in Fig 1(a). The $\varepsilon_2(\omega)$ spectra of the two compounds are found to be somewhat similar. The minor differences are most likely due to differences in conduction bands and wave function symmetries, which require that the selection rules be fully reflected in the matrix moment elements. The calculated ε_2 spectra show two structures in $AsNMg_3$ and three structures in $SbNMg_3$. In $SbNMg_3$, the magnitude of the main peaks is smaller. The peaks are caused by inter band transitions from occupied hybridized As, Sb, and N p states to unoccupied hybridized As, Sb, and Mg s states. It should be noted that because the density functional theory underestimates the band gap of semiconductors, the calculated positions of the structures in the optical spectra of the compounds may be smaller than the experimental values, which are currently unavailable. The values of the main peaks in the $\varepsilon_1(\omega)$ spectra for the real part of the dielectric function shown in Fig. 1(b) are approximately 2.8 and 2.70 eV in $AsNMg_3$ and $SbNMg_3$ semiconductors, respectively. The overall spectral profile is similar, with $AsNMg_3$ and $SbNMg_3$ passing through global minima at 6.4 and 5.5

Table 1. Summary of structural models and parameters proposed for the room-temperature phase of Li_2OHCl

Study	Space group	Symmetry	Lattice parameters	Model available	Comments
Barlage and Jacobs	Pmma	Orthorhombic	a = 7.680 Å, b = 4.001 Å, c = 3.899 Å	No	X-ray diffraction study
Eilbracht	—	Orthorhombic	—	No	Neutron diffraction study. Weak superstructure reflections and small orthorhombic splitting identified
Schwering	Amm2	Orthorhombic	a = 3.8220 Å, b = 7.9968 Å, c = 7.7394 Å	No	X-ray diffraction study
Song	Pmmm	Orthorhombic	a = 3.8945 Å, b = 3.9937 Å, c = 7.6634 Å	No	In situ X-ray diffraction study. Structure observed at 26 °C
Song	P4mm	Tetragonal	a = b = 3.9129 Å, c = 3.9188 Å	No	In situ X-ray diffraction study. Structure observed at 40 °C
Howard	P4mm	Tetragonal	a = b = 3.794 Å, c = 3.578 Å	Yes	DFT predicted ground-state structure using non-standard coordinates
Howard	$Pmc2_1$	Orthorhombic	a = 3.831 Å, b = 3.617 Å, c = 7.985 Å	Yes	DFT predicted metastable structure state
Howard and Holzwarth	Cmcm	Orthorhombic	a = 7.91 Å, b = 7.74 Å, c = 7.42 Å	Yes	DFT predicted structure
Hanghofer	Pban	Orthorhombic	a = 7.74574 Å, b = 7.99730 Å, c = 3.8229 Å	Yes	Neutron diffraction study. Sample not deuterated. Structure refined at both 300 and 4 K. Parameters shown for data obtained at 300 K
Hanghofer	Pmmm	Orthorhombic	a = 7.74898 Å, b = 8.00215 Å, c = 3.8251 Å	Yes	Neutron diffraction study. Sample not deuterated. Structure refined at both 300 and 4 K. Parameters shown for data obtained at 300 K

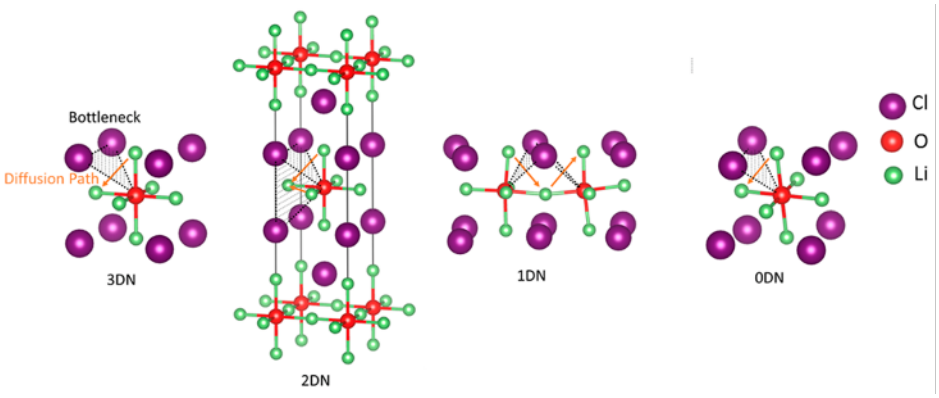

Figure 2. Schematic illustrating the Li diffusion in anti-perovskites through the Cl−O−Cl triangular bottleneck.[66] Reproduced with permission from ref 32. Copyright 2021 ACS

eV, respectively[19].

The calculated optical reflectivity for the compounds is shown in Fig. 1(c). It is observed that the reflectivity of these compounds increases up to about 10.0 eV before decreasing. $SbNMg_3$ has a slightly higher reflectivity on average, with a maximum value of around 62%. The maximum reflectivity of these compounds occurs between 5 and 10.0 eV, which is in the ultra violet range. As a result, the compounds may be used as ultraviolet radiation shields. Figure 1(c) depicts the calculated optical reflectivity of the compounds. The reflectivity of these compounds is observed to increase up to about 10.0 eV before decreasing. $SbNMg_3$ has a slightly higher average reflectivity, with a maximum value of around 62%. These compounds' maximum reflectivity occurs between 5 and 10.0 eV, which is in the ultra violet range. As a result, the compounds have the potential to be used as ultraviolet radiation shields. The electron energy loss function $(-\mathrm{Im}\ \varepsilon-1)$ shown in Fig. 1(d), is another important optical property calculated in this work. It is worth noting that the plot of the energy loss function in these compounds lacks a sharp peak. The peak's energy is typically assigned to the energy of volume plasmon, $\hbar\omega p$. Because there is no well-defined peak in $AsNMg_3$, we assume the $\hbar\omega p$ is in the range 15.3-18.0 eV. The value for $SbNMg_3$ is approximately 16.3 eV[10,18,27,37,42,51,55,61,69].

Wang et al created $BaMQ_3X$ (M = As, Sb; Q = S, Se; X = Cl, Br, I) using Solid-state reactions, which crystallizes in the space group Pnma. UV-vis diffuse reflectance spectroscopy was used to investigate the optical absorption properties of these compounds, and band gaps were determined using an extrapolation method. The optical band gap of Ba_2AsS_3X (X = Cl, Br, I) is 2.80 eV, which is consistent with their pale-yellow color. The optical band gap of Ba_2AsSe_3X (X = Br, I) is 2.28 eV. Ba_2SbS_3I has an optical band gap of 2.64 eV and is pale yellow. The similar band gaps of Ba_2AsS_3X (X = Cl, Br, I) and Ba_2AsSe_3X (X = Br, I) indicate that the band edges of these compounds are primarily contributed by As-Q bond states, whereas the states of the more ionic halogens are located deeper in the valence band[46].

Electric properties of Anti-perovskites

In the last decade, researchers have paid close attention to anti-perovskites[27]. Primary reasons for choosing these materials are their industrial utility[60]. Because anti-perovskites have good thermoelectric (TE) properties, they have enormous potential to solve the energy crisis. Waste heat is directly converted to electrical energy in thermoelectric systems. To achieve high efficiency, researchers are looking for suitable materials for thermoelectric generators. Band gaps in good thermoelectric materials are typically large enough to have a high Seebeck coefficient but small enough to have a high electrical conductivity[42].

Lithium-based anti-perovskites have shown potential as ionic conductors due to their large voltage stability window and chemical stability in conjunction with lithium metal, as well as acceptable ionic conductivity, prompting researchers to investigate their alkali metal counterparts[37,61]. The general composition of anti-perovskites is X_3AB, where X is an alkali ion (Li, Na, K), A is the smaller of two anions (typically O, S, or Se), and B is a larger anion such as a halogen (F, Br, Cl, I) or cluster anion (BH_4, NO_2), are being investigated as potential fast-ion conductors for solid state batteries[51].

So far, Li-based solid electrolytes have shown superionic conductivity, low activation energy, and very low electronic conductivity, as well as the potential for a wide operation window in voltage and current. For Lithium-rich anti-perovskites (LiRAP) room temperature ionic conductivity is greater than 10^{-3} S/cm and activation energy of 0.2-0.3 eV. As the temperature approaches the melting point, the anti-perovskites' ionic conductivity increases to advanced superionic conductivity of > 10^{-2} S/cm and beyond. It is not surprising that there is a large body of literature dedicated to increase in ionic conductivity, decrease in activation energy, and comprehending the underlying mechanistic features of ion transport in fast ion conductors (Figure 3)[38].

The anti-perovskite family of solid electrolytes is no exception, as shown in Table 2, which summarizes the reported ionic conductivities and activation energies (from both experiment and modeling) for a wide range of anti-perovskites. Many anti-perovskite materials contain a group II-A element at the face center of the unit cell, resulting in octahedral coordination. Chern et al. created the calcium-based anti-perovskite material $BiNCa_3$ by combining and pressing Ca_3N_2 and Bi powders into a pellet and then heating the pellet at 1000 C in flowing, dry N_2 gas[41]. The authors found the same result when they substituted Bi for other trivalent elements such as P, As, Sb, Ge, Sn, and Pb. According to the authors, all of these materials have cubic structures with the exception of $PNCa_3$ and $AsNCa_3$, which have distorted orthorhombic structures due to their small P_3 and As_3 atomic sizes. $PbNCa_3$, $SnNCa_3$, and $GeNCa_3$ materials are metallic in nature, while $BiNCa_3$ and $SbNCa_3$ are semiconductors with small band gaps, and $AsNCa_3$ and $PNCa_3$ exhibit insulating behavior with structural phase transitions[47].

Amara et al. investigated the structural, elastic, and electronic properties of $PNMg_3$, $AsNMg_3$, $SbNMg_3$, and $BiNMg_3$ within the GGA, while treating the exchange and correlation effects by the Tran-Blaha mBJ potential for the band structure, density of states, as well as charge density to achieve better results[18] This is the first study on anti-perovskite materials based on $PNMg_3$ and $BiNMg_3$. Semi conductiv-

ity is present in all materials. $PNMg_3$ and $AsNMg_3$ are direct band gap materials, while $SbNMg_3$ and $BiNMg_3$ are indirect band gap materials, according to Table 2[18]. Because of the use of mBJ potential, the authors achieved the highest band gap values compared to previous studies. The elastic properties show that $PNMg_3$ is the hardest material, while $BiNMg_3$ is the softest. A relatively strong hybridization of Pb-6p with O-2p is seen in X_3PbO (X = Ba, Sr, and Ca), close to the conduction band minima, with only a minor contribution from the associated Ba-6s, Sr-5s, and Ca-4s states. The valence band maxima in all three anti-perovskites are primarily made up of Pb-6p[7]. $AlCTi_3$ was examined using transmission electron microscopy by Tian and Nemoto. The physical characteristics of this material, including its electronic, mechanical, and thermal properties, were subsequently studied by various researchers using various techniques[37,46]. Using GGA potential, Yu-Lei investigated this material's electronic characteristics. The author's band structure demonstrates that this substance is metallic.

For a better understanding of the various states at the Fermi level, the density of states is also discussed. The structure of Ti_3AlC is stabilized by the strong hybridization between Ti-3d and Al-3p states as well as between Ti-3d and C-2p states. First principal calculations were used by Medkour et al.[29] to examine the structural, elastic, and electronic characteristics of $ACTi_3$ (A = Al, In, and Tl) anti-perovskites materials. All of these materials have metallic appearance with strong mixed ionic and covalent bonds. According to the authors, as the antibonding state between the Ti and A atoms increases, stiffness decreases[47].

By computing the band structures and the total and partial density of states (DOS) along highly symmetric directions in the first Brillouin zone, the electronic properties of the investigated cubic anti-perovskites compounds X_3ZN (X = Ca, Sr, Ba; Z = As, Sb, Bi) have been discussed. Three different exchange-correlation functionals, PBE-GGA, EV-GGA, and TB-mBJ, were used to implement band gap calculations. The band structure data are used to determine the electronic properties. The electronic band structure reveals that all the compounds have a direct band gap nature. TB-mBJ predicted larger bandgaps compared to the other functionals because of its semi local nature. The compounds show high absorption peaks and optical conductivity in the ultraviolet region. Therefore, these compounds are very useful for high frequency optoelectronic devices[29].

According to the calculated energy band structure for $TlNCa_3$, there is no band gap at the Fermi level and the valence and conduction bands heavily overlap in the high symmetry directions of the Brillouin zone. This discovery demonstrates the metallic nature of the material and is consistent with the outcomes of the LDA LMTO-ASA[43] experiment. For the polycrystalline $TlNCa_3$, the sound velocity and Debye temperature have been calculated. The band structures demonstrate the metallic nature of this compound. The PDOS study show that Tl-6p states are responsible for the conductivity in $TlNCa_3$. In contrast to the Ca-Tl bond, the charge transfer and charge density distribution map analysis reveals that the Ca-N bond is a mixture of ionic-covalent character[60].

Bouhemadou and coauthors[10] investigated the structural, elastic, electronic, and optical properties of $AsNMg_3$ and $SbNMg_3$ materials using pseudopotential plane waves method (PP-PW) within the generalized gradient approximation (GGA). For $AsNMg_3$ the fundamental direct band gap initially increases up to 4 GPa and then decreases as a function of pressure, concurrently retaining its direct band gap nature in entire pressure range applied, while $SbNMg_3$ shows transition from fundamental indirect band gap to direct band gap nature as pressure reaches 6.85 GPa as shown in Figures 4(a) and 4(b).

Elastic properties of Anti-perovskites

In addition to electromagnetic response of given solids, the knowledge of elastic properties, aids in determining the suitability of a given material for a specific application. The elastic properties of solids are fundamentally related to many basic solid-state properties, such as equation of the state (EOS), specific heat, thermal expansion, Debye temperature, Grüneisen parameter, melting point, and many others.

Currently, a set of anti-perovskite-type Ni-rich nitrides $MNNi_3$ (where M stands for Zn, Cd, Mg, Al, Ga, and In) has been synthesized and (or) characterized using band structure calculations[9]. For cubic Ni-rich nitrides, many intriguing physical properties have been reported. To gain systematic understanding of elastic parameters, a comparative first-principles study of synthesized and hypothetical cubic Ni-rich nitrides $MNNi_3$ (where M are Zn, Cd, Mg, Al, Ga, In, Sn, Sb, Pd, Cu, Ag, and Pt) have been performed. The calculations have been carried out using FLAPW method within the generalized gradient approximation (GGA). In order to estimate the values of three independent elastic constants (Cij) for cubic phases of $MNNi_3$, stress tensors on strains applied to equilibrium structure were calculated. For cubic $MNNi_3$ phases, the values of the independent elastic constants Cij are positive and satisfy the generalized criteria[34] for mechanically stable crystals, which are $(C_{11}-C_{12}) > 0$, $(C_{11}+2C_{12}) > 0$, and $C_{44} > 0$. The only exception is $SbNNi_3$, which has mechanically unstable, so further discussion of its elastic properties will be skipped. For isostructural $MNNi_3$ phases, there are no universal correlations between structural parameters and elastic moduli (B, G and $\acute{G}$). This lack of correlation is likely due to the fact that different M atoms

Table 2. Reported ionic conductivities and activation energies (from both experiment and modeling) for a wide range of anti-perovskites

Composition	Conductivity (S cm^{-1})	Activation energy (eV)	Study
Li_3OCl	0.85×10^{-3} (RT) 4.82×10^{-3} (523 K)	0.26	Zhao and Daemen
	0.12×10^{-3} (300 K) 4.58×10^{-2} (480 K)	—	Zhang
Li_3OCl (thin film)	8.9×10^{-6} (RT) 2.0×10^{-4} (RT)	—	Lü Lü
Li_3OCl (PLD target)	5.8×10^{-7} (RT)	—	Lü
Li_3OCl (glassy)	2.5×10^{-4} (RT)	—	Heenen
Li_3OBr	5.36×10^{-2} (450 K)	—	Zhang
Li_3OA (A = Cl or Br)	$\sim 5 \times 10^{-3}$ (500 K)	0.27–0.31	Dawson
$Li_3OCl_{0.5}Br_{0.5}$	1.94×10^{-3} (RT) 6.05×10^{-3} (523 K)	0.18	Zhao and Daemen
	0.21×10^{-3} (300 K)	—	Zhang
	3.56×10^{-3} (500 K)	~0.30	Dawson
$Li_3OCl_{1-x}Br_x$ ($0 < x < 1$)	$0.7–2.5 \times 10^{-5}$	0.37–0.39	Deng
	3×10^{-5} (473 K)	0.97	Hartwig
	$\sim 10^{-4}$ (323 K)	~0.56–0.88 (impedance)	Schwering
Li_2OHCl		~0.26–0.46 (^7Li NMR)	
	$\sim 1.7 \times 10^{-4}$	0.41	Dawson
	—	0.57 (cubic) 1.80 (orthorhombic)	Song
	0.16×10^{-3} (373 K)	0.48	Effat
	1.2×10^{-8} (310 K)	0.64	Wang
	1.4×10^{-6} (312 K)	0.55	
$Li_{3-x}OH_xCl$ ($x = 0.2–1$)	—	0.24–0.26	Song
	—	0.30–0.42	Dawson
$Li_2(OH)_{0.9}F_{0.1}Cl$	3.5×10^{-5} (298 K) 1.9×10^{-3} (373 K)	—	Li
	0.05×10^{-3} (298 K) 0.94×10^{-3} (373 K)	0.40	Effat
$Li_2OHF_{0.1}Cl_{0.9}$	0.38×10^{-3} (298 K) 4.78×10^{-3} (373 K)	0.35	Effat
Li_2OHBr	5×10^{-5} (473 K)	—	Hartwig
Li_3SI	—	0.27 (vacancy) 0.16 (interstitial)	Wang
Li_6OSI_2	1.03×10^{-3} (300 K) 5×10^{-3} (300 K)	0.26 (vacancy) 0.22 (interstitial)	Wang
Li_3SBF_4	0.14×10^{-2} (RT)	0.21	Fang
$Li_3SCl_{0.5}(BF_4)_{0.5}$	$>10^{-1}$	~0.18–0.30	Fang
$Li_3OCl_{0.5}(BH_4)_{0.5}$	$\sim 10^{-4}$ to 10^{-1} (RT)	—	Fang

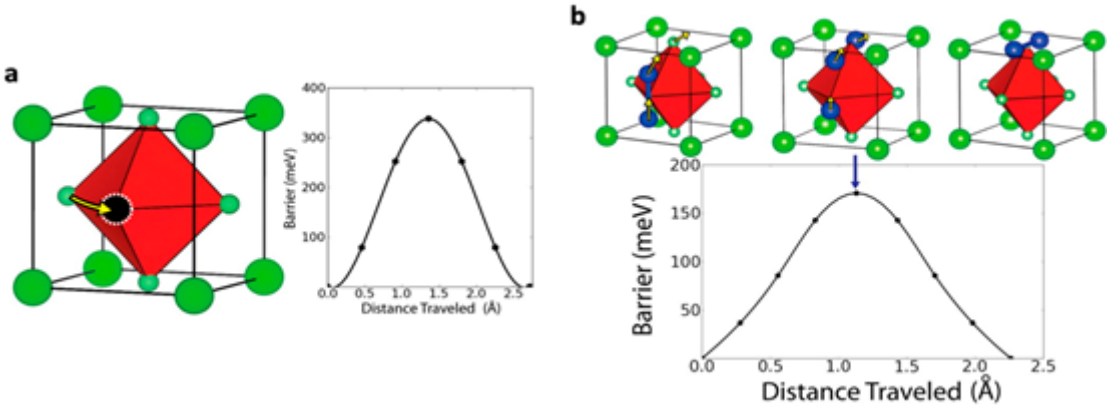

Figure 3. (a) Lithium migration into a vacant site (black with dotted white line). (b) Li ions migrate through Frenkel defects.[3] *Reproduced with permission from ref 49. Copyright 2013 American Chemical Society.*

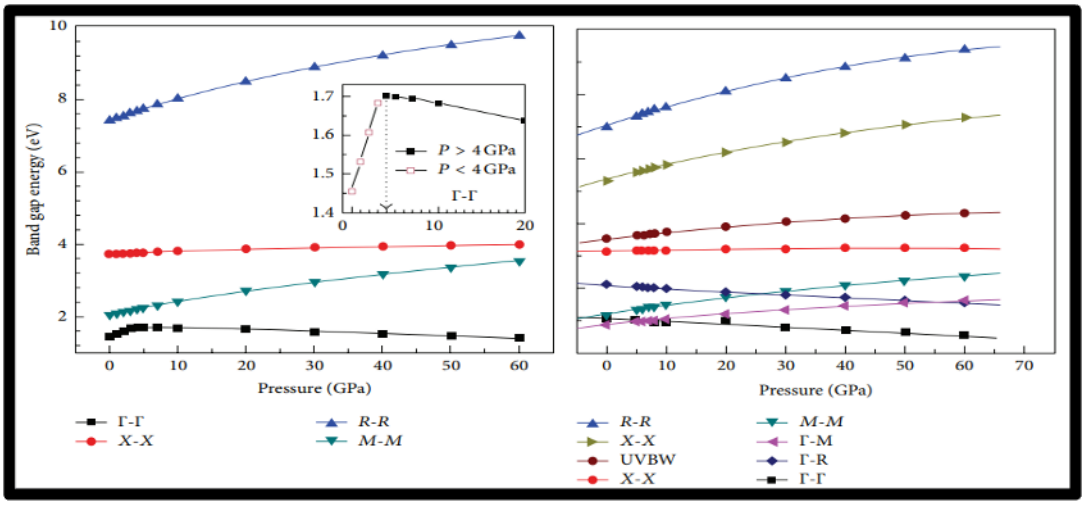

Figure 4. Direct and indirect band gap energies and upper valence bandwidth versus pressure for (a) $AsNMg_3$ and (b) $SbNMg_3$. [10] *Reproduced with permission from ref. 30. Copyright 2015 Hindawi Publishing Corporation.*

play essentially different roles in the formation of the inter-atomic bonding in these anti-perovskites. B>G'>G indicates that the shear modulus G is the factor limiting the mechanical stability of the majority of $MNNi_3$ phases. However, the limiting parameter for the $InNNi_3$ and $PdNNi_3$ phases B>G>Ǵ i.e., here, is the tetragonal shear modulus Ǵ[35].

$TlNCa_3$ belongs to the class of ternary calcium nitrides. The $TlNCa_3$ compound has received less attention than the other members of this family. Few studies have been conducted to investigate its properties. The structural, elastic, and electronic properties of cubic anti-perovskite-type $TlNCa_3$ were investigated using a pseudo potential plane-wave approach based on density functional theory in both the generalized gradient and local density approximations. $TiNCa_3$ is predicted to have the same hardness as the other $ANCa_3$ compound family[56]. This conclusion is supported by the behavior of the shear modulus G. Certainly, a material's hardness is defined as its resistance to another material penetrating its surface, and this resistance is determined by dislocation mobility. Thus, the response of interatomic bonds to shear strain is one of the determinants of hardness[25]. $TlNCa_3$ has the same shear modulus value as the other $ANCa_3$ compounds in the family[56]. For covalent materials, the Poisson's ratio (σ) is small (σ= 0.1), whereas for ionic materials, the typical value is 0.25[25]. Using the GGA (LDA), the calculated value of for $TlNCa_3$ is around 0.224 (0.233), implying that $TlNCa_3$ has a higher ionic contribution in intra-atomic bonding. Further it can be evaluated that the calculated B, G, E, and λ increases with increasing pressure, implying that the toughness of $TlNCa_3$ can be improved under high pressure. $TlNCa_3$ may be classified as brittle material because the calculated value of B/G is less than the critical value sug-

Table 3. Elastic Moduli and Pugh Ratios of Li_3OCl, Li_2OHCl, $Li_2(OH)_{0.9}F_{0.1}Cl$, and $Li_2OHF_{0.1}Cl_{0.9}$ Anti Perovskites

electrolyte	B bulk modulus (GPa)	G shear modulus (GPa)	E Young's modulus (GPa)	G/B Pugh ratio
Li_3OCl	57.2	42.9	103	0.75
Li_3OCl	55.7	41.5	99.7	0.74
Li_2OHCl	27.6	17.4	43.1	0.63
$Li_2(OH)_{0.9}F_{0.1}Cl$	26.1	17.6	43.2	0.67
$Li_2OHF_{0.1}Cl_{0.9}$	20.2	13.5	33.1	0.67

gested by Pugh[60].

The systematic trends for the elastic properties of the anti-perovskites $MCNi_3$ are evaluated for the first time. The generalized criteria[6] for mechanically stable crystals are satisfied by all independent elastic constants Cij for $MCNi_3$ phases. The cubic MCNi3's bulk modules increase in the following order: B(CdCNi3) < B(MgCNi3) < B(ZnCNi3). For all anti-perovskites $MCNi_3$, the shear modules G limit the mechanical stability of these materials. Using these data, numerical estimates of a set of elastic parameters (bulk and shear modulus, Young's modulus Y, Poisson's ratio (m), Lame's coefficients (l, k)) of the polycrystalline $MCNi_3$ species are performed using the Voigt-Reuss-Hill (VRH) approximation. This is the first quantitative theoretical prediction of superconductive $MCNi_3$ ceramics' elastic properties[6].

Superconductivity

Ni_3MgC, which was found in 2001, was the first anti-perovskite to exhibit superconductivity[31]. When examining the superconducting mechanism, the cubic Ni_3MgC represents an s-wave BCS-type type-II superconductor, providing a unique example to the non-cuprate superconductor $Ba_{1-x}K_xBiO_3$. As a result, in-depth experimental and theoretical research was done on superconductors related to Ni_3MgC, including Ni_3CuN, Ni_3ZnN, Cr_3GaN, and K_2NiF_4-type layered A_2CNi_4 (A = Al, Ga, Sn)[1,32]. The high Ni content of the crystal structure suggests that the development of superconductivity may be greatly influenced by magnetic interactions. To determine the contributions of the local structure, electronic states, and electron-phonon interactions to the superconductivity, measurements of the Ni K-edge X-ray absorption, the 13C NMR, and theoretical computational simulations were carried out. By increasing the x value in Ni_3MgCx, T_c could be experimentally improved slightly, but it decreased when the Ni site was doped with other transition metals like Mn, Fe, Co, and Cu.

Superconductivity was also discovered in the so-called anti-post perovskites V_3PnNx (Pn = P, As)[4]. These compounds crystallize in the filled Re_3B structure, and the positions occupied by the cations and anions are the reverse of those in the post perovskite structure. The anti-post perovskites V_3PnNx are composed of alternately stacked NV_6 octahedral layers and Pn layers, creating a quasi-2D electronic state. V_3PN and V_3AsN exhibit bulk superconductivity at T_c = 4.2 and 2.6 K, respectively. At 1.8 K, the magnetization isotherms exhibit typical type-II superconducting behavior. The presence of superconductivity in N-deficient V_3PnN_x suggests that the 3d electrons of V are primarily responsible for the emergence of superconductivity. The highest Tc measured in $V_3PN_{0.9}$ is 5.6 K[45].

Another intriguing example of an anti-perovskite-based structure closely related to the heavy fermion superconductor Pt_3CeSi is the family of ternary platinum phosphides Pt_3AP (A = Ca, Sr, La)[21]. With the highest critical temperature of T_c = 8.4 K for Pt_3SrP,[68] all three compounds exhibit superconductivity at low temperatures, as shown by their resistivity, diamagnetic transitions, and specific heat jumps at these temperatures. The experimental results on Pt_3SrP show that the charge carriers in the multiple Fermi surface pockets strongly couple with the low-lying phonons, resulting in strong coupling superconductivity at a relatively high temperature of 8.4 K. Multiple Fermi surface pockets may also improve electron-phonon coupling by increasing the prospect of Fermi surface nesting and phonon softening, which is coherent with the differing superconducting properties of Pt_3LaP and Pt_3SrP, which have different Fermi surface topologies. The experimental results on Pt_3SrP shows that the charge carriers in the multiple Fermi surface pockets strongly couple with the low-lying phonons, resulting in strong coupling superconductivity at a relatively high temperature of 8.4 K. Multiple Fermi surface pockets may also improve electron-phonon coupling by increasing the likelihood of Fermi surface nesting and phonon softening, which is coherent with the differing superconducting properties of Pt_3LaP and Pt_3SrP, which have different Fermi surface topologies[45].

Sr_3SnO was the first superconducting anti-perovskite oxide, with a T_c of around 5 K. Dirac points in Sr_3SnO's electronic structure result from the inversion of bands with different parities. Based on theoretical analysis, it was proposed that topological odd-parity superconductivity, analogous to superfluid 3He-B, could exist in moderately hole-doped Sr_3SnO due to unusual orbital texture on the Fermi surface. The discovery of a new class of inverted valence oxide superconductor will stimulate research into topological materials science based on a variety of anti-perovskite oxides[54].

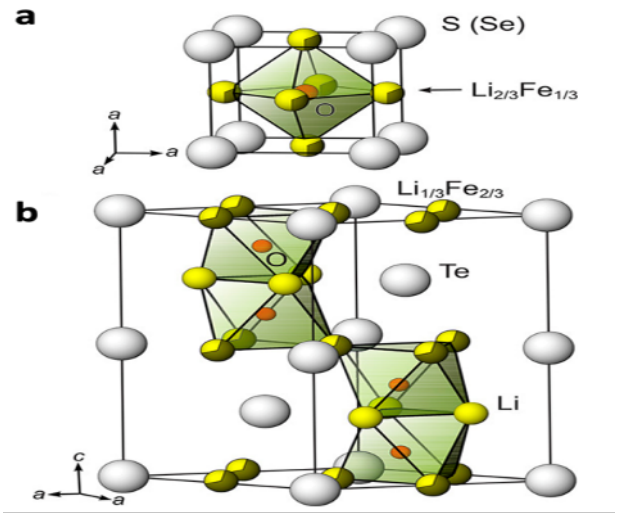

Figure 5. Crystal structures of $(Li_2Fe)ChO$ (Ch = S, Se, Te). (a) Cubic anti-perovskites $(Li_2Fe)ChO$ (Ch = S, Se) and (b) 4H-hexagonal anti-perovskite $(Li_2Fe)TeO$.[50] Reproduced with permission from ref 30. Copyright 2017 American Chemical Society.

Magnetic properties of Anti-perovskites

Magnetic perovskite oxides ABO_3 are widely used in modern devices such as storage devices, magnetocaloric effects, and magneto resistivity. Magnetic anti-perovskites $M_3M'X$ (M = Mn, Fe, etc.; M′ = Ga, Al, Zn, In, Sn, etc.; X = N, C) have also received considerable attention as a promising new class of magnetic materials. Mn-based magnetic anti-perovskites are the most appealing among them because of their recently reported giant magnetoresistance (GMR)[44,63] massive magnetocaloric effect (MCE)[65,67] and giant magnetostriction (MS)[40]. Furthermore, these $Mn_3M'X$ anti-perovskites are metallic, indicating good electrical, thermal, and mechanical conductivity.[26] Mn_3GaC is a GMR prototype compound that cools to three magnetic transitions: a paramagnetic (PM) to ferromagnetic (FM) transition at T_C 246 K, an FM intermediate magnetic phase transition (IM) at TF-I 160 K, and an intermediate to antiferromagnetic (AFM) transition at TI-A 158 K. The Mn 3d orbitals contribute to the DOS at the Fermi level in $Mn_3M'X$ anti-perovskites, while the Mn-X p-d orbital hybridization broadens the conduction band across the Fermi level and drives the high conductivity. These Mn 3d electrons take part not only in conduction but also in magnetic exchange interactions. As a result, the 3d electrons' Mn-Mn direct exchange interaction will compete with the Mn-X-Mn magnetic coupling interaction. Furthermore, in terms of magnetic interactions, the 3D network built by corner-sharing Mn_6X octahedra contains 3D geometrical frustration[39]. $Mn_3M'A$ is sensitive to subtle changes in chemical composition, temperature, pressure, and external magnetic field due to strong couplings among the various degrees of freedom and competing magnetic interactions[39]. Mn_3GaC has GMR curves that are plateau-like versus temperature from 135 to 165 K, with a maximum MR of 50% at 5 T[2]. The GMR is associated with the field-induced AFM-FM/IM transition, in which the lattice, spin, and charge have a strong correlation. If the AFM ground state can be effectively suppressed by an external magnetic field, a GMR with a larger temperature span may be observed. To suppress the AFM ground state, a magnetic field as strong as 240 kOe is required.

Figure 5. Illustrates crystal structures of $(Li_2Fe)ChO$ (Ch = S, Se, Te). (a) Cubic anti-perovskites $(Li_2Fe)ChO$ (Ch = S, Se) and (b) 4H-hexagonal anti-perovskite $(Li_2Fe)TeO$.

COMPUTATIONAL TECHNIQUES FOR ANTI-PERVOSKITES

The ground states properties of anti-perovskites are observed by using Full-Potential Linearized Augmented Plane-wave Method (FP-LAPW) that is implemented in the light of density functional theory concepts and integrated in Wein2k code. The Kohn–Sham equations are evaluated to compute the Eigen values and the Eigen functions. Generalized Gradient Approximation (GGA) that was anticipated by Wu and Cohen is used to reveal the ground state parameters[60]. The application of mBJ potential evidences that the evaluated electronic properties agree to those revealed by the experiments.

Full-potential Linearized Augmented Plane-wave Method (FP-LAPW

The Full-Potential Linearized Augmented Plane-Waves Method solves the Kohn–Sham equations in the framework of the density functional theory (DFT) to find the ground-state valence electron density of a periodic infinite crystal. The core electrons are treated using an atomic relativistic calculation, under the influence of the valence electrons and the rest of the crystal. Both densities are added up, rendering the total ground-state FPLAPW density for the system.

A FP-LAPW method, as implemented in the Wien2k package, was utilized to obtain the physical properties of the X_3ZN compounds. Following this method, the wave function, potential and charge density were expanded in two different basis sets. The wave function was expanded using spherical harmonics within the atomic spheres, while outside these spheres (interstitial regions), a plane wave basis was used. It is concluded from the results that calculated structural parameters are in good agreement with available experimental data. The lattice constant varies inversely to the bulk moduli of the compounds. The electronic band structure reveals that all the compounds have a direct band gap nature. TB-mBJ predicted larger bandgaps compared to the other functionals because of its semi local nature. The compounds show high absorption peaks and optical conductivity in the ultraviolet region.

Plane wave Pseudo-Potential (PP-PW method

Ab initio pseudopotential plane wave (PP-PW) method within the Generalized Gradient Approximation (GGA) and the local density approximation (LDA) is used to study the structural, elastic and electronic properties of the unexplored anti-perovskite $ANTi_3$ compounds. The main results and conclusions can be summarized as follows. The calculated equilibrium lattice constants of these compounds are in reasonable agreement with the available experimental data. Bulk moduli provided from fitting the Birch–Murnaghan EOS of the studied compounds, were obtained by employing dense sampling technology in the low-pressure region, hence our results for B are good and accurate. The B/G values of $ANTi_3$ compounds show that these materials behave as ductile. The band structure calculations show that these compounds are conductors and exhibit magnetism at their equilibrium lattice constants. The bonding charge density calculations and the Milliken charge analysis reveal that the chemical bonding in $ANTi_3$ compounds may be covalent–ionic. The elastic properties of the studied compounds showed a correlation with the bonding properties.

Applications of Anti-perovskite

Anti-perovskite SSEs are expected to find widespread use in energy storage batteries due to a variety of advantages. Furthermore, the low melting point of anti-perovskite SSEs opens up new opportunities, such as thin-film SSEs, composite SSEs, and composite electrodes. Furthermore, anti-perovskite cathode materials with high capacity have a high potential for use in Lithium Ion Battries (LIBs)[2,26,39,40].

Anti-perovskite cathode for LiBs

In recent years, a series of Li_2TMChO (TM = Fe, Co, Mn; Ch = S, Se, Te) anti-perovskite have been developed, in which Li_2FeSO has an ultra-high theoretical capacity over 450 mAh g^{-1} with two lithium-ion extraction[52]. However, the anti-perovskite structure of Li_2FeSO was predicted to collapse after 1.25 lithium-ion extraction with the capacity of 283 mAh g^{-1} [24]. The half cells with Li_2FeSO cathode and lithium metal anode in ether-based electrolyte possessed a high capacity of about 275 mAh g^{-1} at a rate of 0.1 C. The high capacity of Li_2FeSO is mainly derived from the redox reaction of Fe_2+/Fe_3+ at low potentials, while S is involved at higher cell voltage, indicating the bifunctional battery chemistry of Li_2FeSO. In contrast, Li_2FeSO/Li half cells using carbonate-based electrolyte showed lower capacity but higher cycling stability that remained a capacity of 120 mAh g^{-1} at 0.1 C after 50 cycles[11]. However, the equilibrium voltage of anti-perovskite cathode Li_2TMChO versus Li/Li+ is below 3 V, which is generally lower than that of the current typical cathode, such as $LiMO_2$ (M = Ni, Co, Mn). The low average voltage results in lower energy density compared to the commercial LiBs. Therefore, the electrochemical performance of the anti-perovskite cathode has to be further optimized for the practical applications.

Lithium-ion battery electrolytes

To take advantage of each component's advantages, hybrid electrolytes made up of different ionic conductors may be the best option. Inorganic/organic hybrid electrolytes, inorganic/polymer hybrid electrolytes, and hybrid quasi-solid-state electrolytes are examples of hybrid electrolytes. An ultrathin Li_3OCl quasi-solid-state electrolyte to cover the Li-metal anode was recently proposed by Yan et al[13]. In order to improve interfacial contact and enable quick Li+ transport in both electrolytes and electrodes, Li_3OCl was wetted with a liquid electrolyte. Despite being significantly safer than conventional liquid systems, hybrid quasi-solid-state electrolytes still have safety concerns because they use liquid electrolytes. Due to their high ionic conductivity, good flexibility, and low interfacial resistance with electrode, inorganic/polymer hybrid solid electrolytes have also received a lot of attention. These electrolytes are made up of an inorganic ionic conductor and a solid polymer electrolyte. Li_2OHBr/PEO (poly ethylene oxide) hybrid solid electrolytes have recently been reported

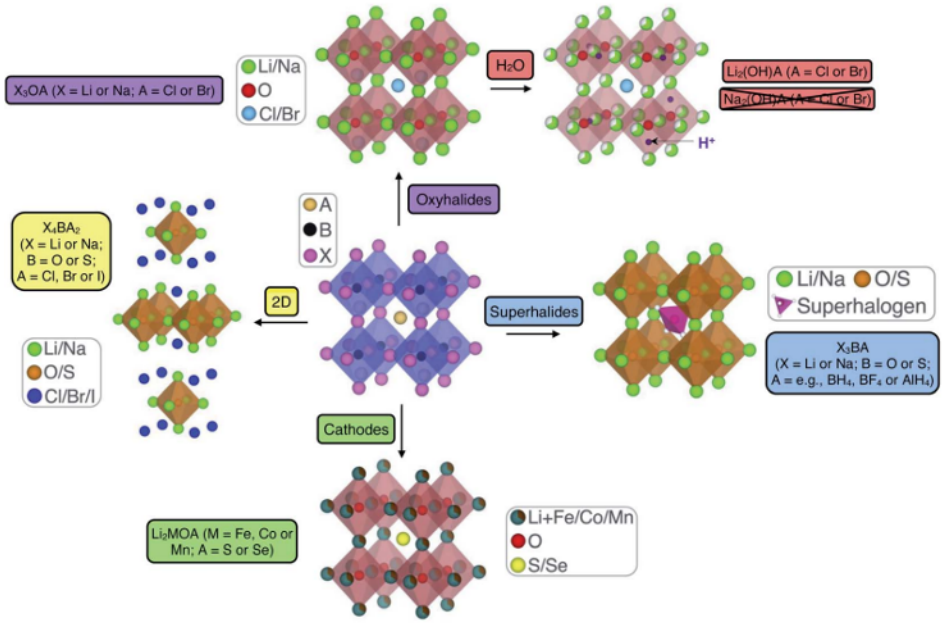

Figure 6. Schematic highlighting the structural and compositional versatility of anti-perovskite battery material.[5] *Reproduced from Ref. 68 with permission from the Royal Society of Chemistry. Copyright 2021 Royal Society of Chemistry.*

to have improved mechanical strength and Li+ conductivity compared to PEO polymer electrolyte[23]. Figure 6 demonstrates schematic highlighting of the structural and compositional versatility of anti-perovskite battery material[5] **.**

For thin-film batteries Film SSEs

Most studies show that the thickness of inorganic SSEs is greater than 500 m, which is insufficient for practical applications. The electrolyte layer must be as thin as possible to improve energy and power density. Reduced SSE layer thickness to less than 100 m is a basic requirement for SSEs to compete with commercial LIBs. Because of their low melting point, anti-perovskite SSEs can be easily tailed to a small thickness (5-25 m) by adjusting the amount of molten SSE, resulting in high-energy-density ASSLMBs. Thin film deposition techniques can also reduce the thickness of the anti-perovskite SSE to hundreds of nanometers[50]**.** The PLD-prepared anti-perovskite Li_3OCl film had a high RT ionic conductivity of 2104 S cm^{-1}, and the assembled $LiCoO_2/Li_3OCl$/graphite all-solid-state thin-film battery had an initial discharge capacity of about 120 mAh/g. It demonstrated the high potential of anti-perovskite SSEs for use in thin film batteries. However, for commercial applications, electrochemical performance in thin-film batteries must be improved further. Figure 7 presents a schematic summary of Li- and Na-anti perovskite compositions that have been successfully synthesized, attempted and predicted so far (see also Table 1). This representation makes it apparent that the tolerance factor is not an adequate descriptor of stability for anti-perovskite battery materials.

Experimental and computational studies of electrode-anti-perovskite solid electrolyte interfaces is shown in Figure 8. Figure 8 (a) represents SEM image of Li/Li2OHCl/Li symmetric cell after 160 charge/discharge cycles showing the cross section of the SEI[62]**.** Figure 8 (b) represents EDS mapping of melt-infiltrated NCM (top left), graphite (top right) and $Li_4Ti_5O_{12}$ electrodes (bottom left) and the cross-section of the all-solid-state battery cell, where purple represents combined Ni/Co/Mn, black represents C (graphite), red represents combined Ti/O ($Li_4Ti_5O_{12}$) and the green colour represents Cl from $Li_{1.9}OHCl_{0.9}$ (SSE)[74] . Figure 8 (c) demonstrates relaxed structure of Cl- and O-terminated interfaces consisting of seven layers of Li_3OCl (100) and bcc Li (100) planes[73] .

Electrolyte melt-infiltration for the production of ASSLBs

Xiao et al. created an electrolyte melt-infiltration technology using anti-perovskite SSEs to fabricate ASSLBs with NCM111 cathode and LTO/graphite anode by taking advantage of the low melting point of these materials[23]. Two melt-infiltrated electrodes were then hot-pressed together. The anti-perovskite SSE powder layer that was on top of the slurry-cast electrode was heated to melt and infiltrate into the electrode. The interfacial resistances were reduced as a result of the close contact between the active material NCM111 particles and the melt-infiltrated anti perovskite SSE $Li_{1.9}OHCl_{0.9}$. The manu-

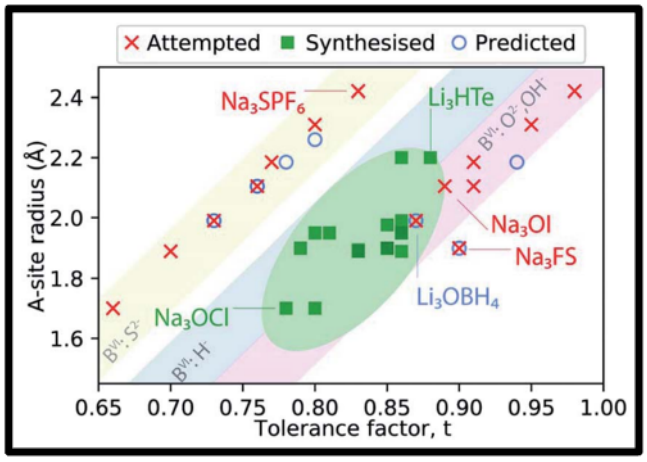

Figure 7. Schematic summary of Li- and Na-anti perovskite compositions that have been successfully synthesized, attempted and predicted[5]. Reproduced from Ref.68 with permission from the Royal Society of Chemistry. Copyright 2021 Royal Society of Chemistry.

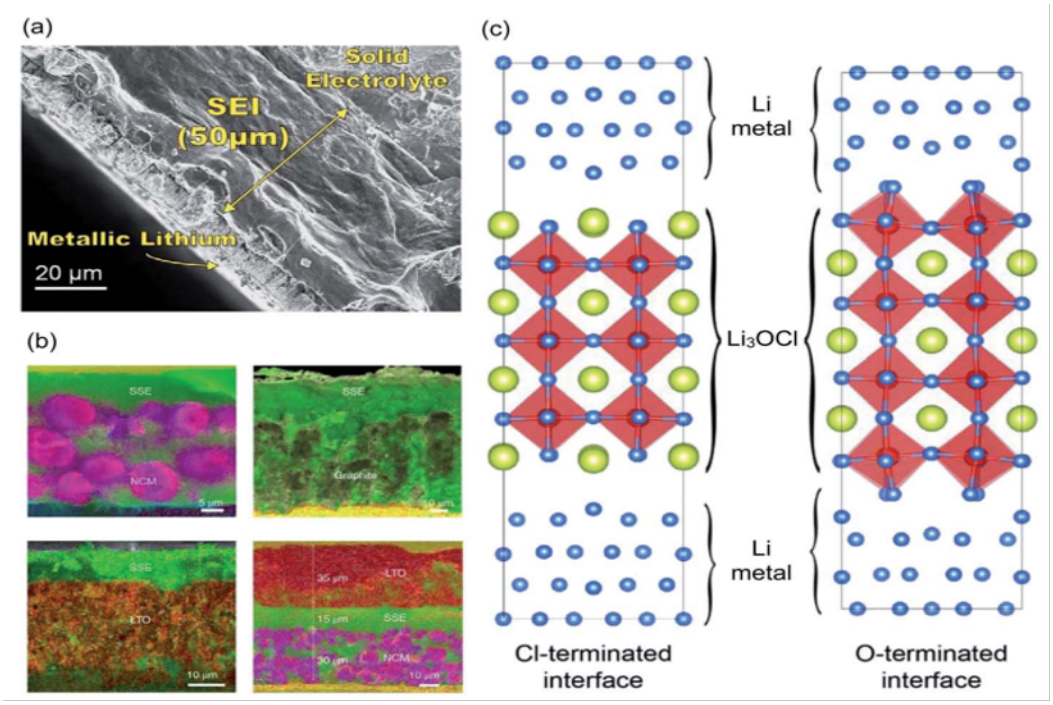

Figure 8. Experimental and computational studies of electrode-anti-perovskite solid electrolyte interfaces. (a) SEM image of Li/Li_2OHCl/Li symmetric cell after 160 charge/discharge cycles showing the cross section of the SEM[62]. Reproduced with permission from ref. 69 Copyright (2016) American Chemical Society. (b) EDS mapping of melt-infiltrated NCM (top left), graphite (top right) and $Li_4Ti_5O_{12}$ electrodes (bottom left) and the cross-section of the all-solid-state battery cell, where purple represents combined Ni/Co/Mn, black represents C (graphite), red represents combined Ti/O ($Li_4Ti_5O_{12}$) and the green colour represents Cl from $Li_{1.9}OHCl_{0.9}$ (SSE).[74] Reproduced with permission from ref. 70 Copyright (2021) Springer Nature. (c) Relaxed structure of Cl^- and O-terminated interfaces consisting of seven layers of Li_3OCl (100) and bcc Li (100) planes[73]. Reproduced with permission from ref. 71 Copyright (2019) American Chemical Society.

factured ASSLBs NCM111/SSE/LTO and NCM111/SSE/graphite performed well in terms of rate and cycling. The application of low-melting-point anti perovskite SSEs in the mass production of high-dense ASSLBs at low cost and scale using melt-infiltration SSE technology shows great promise. In the meantime, consideration should be given to these materials' thermal stability in batteries at the high processing temperature[23].

LiRAPs Li_3OCl has been used to fill the grain boundary of the oxide electrolytes as a binder to form a continuous ionic conductive network among $Li_{6.75}La_3Zr_{1.75}Ta_{0.25}O_{12}$ (LLZTO) particles in LLZTO/Li_3OCl composite electrolyte, similar to the electrolyte melt-infiltration technology that low-melting-point LiRAPs SSE fills as is well known, the LLZTO SSE pellets must be sintered densely at 1200 degrees Celsius. However, by combining LLZTO/Li_3OCl composite SSE pellets with low-melting-point anti-perovskite SSE, the pellets were produced at a lower temperature of 350 C. Furthermore, when compared to LLZTO SSE, the LLZTO-2 wt% Li_3OCl composite SSE had higher density, higher ionic conductivity, a wider electrochemical window, lower interfacial impedance, and better cycling stability against lithium metal. The $LiFePO_4$/Li ASSLBs produced with LLZTO-2 wt% Li_3OCl composite SSE had stable capacities of 157.5 mAh g and 85.7 mAh g at 0.05 C and 0.5 C, respectively. It demonstrates that LiRAPs SSEs have a high potential for developing low-cost composite SSEs with improved performance for ASSLBs[23].

CONCLUSIONS

In this critical review, we summarize the crystal structures of Li rich anti-perovskite type materials and their structural properties, elastic properties, optical properties, mechanical properties, and electrical conductivity. Anti-perovskite materials are still poorly studied compared to traditional perovskites and they need attention to explore new compounds with an anti-perovskite structure and the new phenomena within them. We highlight significant applications of Anti-perovskites such as in Lithium-ion battery electrolytes, and thin-film batteries. We have also concluded briefly various DFT computational techniques to find out useful properties of Li-rich anti-perovskite superionic conductor $Li_3OCl(100)$ surface.

References

1) Shao, D. F.; Lu, W. J.; Lin, S.; Tong, P.; Jian, H. B.; Pan, X. Y.; Sun, Y. P. First-principles prediction of layered antiperovskite superconductors A2CNi4 (A = Al, Ga, and Sn). *AIP Advances* **2012**, *2* (4), 042167–042167.
2) Kim, W. S.; Chi, E. O.; Kim, J. C.; Choi, H. S.; Hur, N. H. Close correlation among lattice, spin, and charge in the manganese-based antiperovskite material. *Solid State Communications* **2001**, *119* (8-9), 507–510.
3) Emly, A.; Kioupakis, E.; Van Der Ven, A. Phase Stability and Transport Mechanisms in Antiperovskite Li3OCl and Li3OBr Superionic Conductors. *Chemistry of Materials* **2013**, *25* (23), 4663–4670.
4) Wang, B.; Ohgushi, K. Post-perovskite Transition in Anti-structure. *Scientific Reports* **2016**, *6* (1), 1–7.
5) James, A. D.; Theodosios, F.; Karen, E. J. Anti-perovskites for solid-state batteries: recent developments, current challenges and future prospects. *Journal of Materials Chemistry A* **2021**, *9*, 18746–18746.
6) Wang, J. Crystal instabilities at finite strain. *Physical review letters* **1993**, *71*, 4182–4182.
7) Hassan, M.; Arshad, I.; Mahmood, Q. Computational study of electronic, optical and thermoelectric properties of X3PbO (X = Ca, Sr, Ba) anti-perovskites. *Semiconductor Science and Technology* **2017**, *32* (11), 115002–115002.
8) Dawson, J. A.; Famprikis, T.; Johnston, K. E. Anti-perovskites for solid-state batteries: recent developments, current challenges and future prospects. *Journal of Materials Chemistry A* **2021**, *9* (35), 18746–18772.
9) Uehara, M. New anti-perovskite-type superconductor ZnNyNi3. *Journal of the Physical Society of Japan* **2009**, *78* (3), 33702–033702.
10) Muhammad, B.; Jalali-Asadabadi,; Rashid, A.; Iftikhar, A. Electronic Properties of Anti-perovskite Materials from State-of-the-Art Density Functional Theory . *Journal of Chemistry* **2015**, *2015*, 495131.
11) Mikhailova, D.; Giebeler, L.; Maletti, S.; Oswald, S.; Sarapulova, A.; Indris, S.; Hu, Z.; Bednarcik, J.; Valldor, M. Operando Studies of Antiperovskite Lithium Battery Cathode Material (Li2Fe)SO. *ACS Applied Energy Materials* **2018**, *1* (11), 6593–6599.
12) Zhu, Y.; Chen, G.; Zhong, Y.; Chen, Y.; Ma, N.; Zhou, W.; Shao, Z. A surface-modified antiperovskite as an electrocatalyst for water oxidation. *Nature Communications* **2018**, *9* (1), 1–9.
13) Yan, C.; Xu, R.; lei Qin, J.; Yuan, H.; Xiao, Y.; Xu, L.; qi Huang, J. 4.5 V High-Voltage Rechargeable Batteries Enabled by the Reduction of Polarization on the Lithium Metal Anode. *Angewandte Chemie International Edition* **2019**, *58* (43), 15235–15238.
14) Li, S.; Zhu, J.; Wang, Y.; Howard, J. W.; Lü, X.; Li, Y.; Kumar, R. S.; Wang, L.; Daemen, L. L.; Zhao, Y. Reaction mechanism studies towards effective fabrication of lithium-rich anti-perovskites Li3OX (X= Cl, Br). *Solid State Ionics* **2016**, *284*, 14–19.
15) Megaw, H. D. Crystal structure of double oxides of the perovskite type. *Proceedings of the Physical Society* **1946**, *58* (3), 340–340.
16) Wang, Y.; Zhang, H.; Zhu, J.; Lü, X.; Li, S.; Zou, R.; Zhao, Y. Antiperovskites with Exceptional Functionalities. *Advanced Materials* **2020**, *32* (7), 1905007–1905007.
17) Hichour, M.; Khenata, R.; Rached, D.; Hachemaoui, M.; Bouhemadou, A.; Reshak, A. H.; Semari, F. FP-APW+lo study of the elastic, electronic and optical properties for the cubic antiperovskite ANSr3 (A=As, Sb and Bi) under pressure effect. *Physica B: Condensed Matter* **2010**, *405* (7), 1894–1900.
18) Amara, K.; Zemouli, M.; Elkeurti, M.; Belfedal, A.; Saadaoui, F. First-principles study of XNMg3 (X=P, As, Sb and Bi) antiperovskite compounds. *Journal of Alloys and Compounds* **2013**, *576*, 398–403.
19) Okoye, C. First-principles optical calculations of AsNMg3 and SbNMg3. *Materials Science and Engineering: B* **2006**, *130* (1-3), 101–107.
20) Sakuda, A.; Hayashi, A.; Tatsumisago, M. Sulfide Solid Electrolyte with Favorable Mechanical Property for All-Solid-State Lithium Battery. *Scientific Reports* **2013**, *3* (1), 1–5.
21) Takayama, T. Strong Coupling Superconductivity at 8.4 K in an Anti-perovskite Phosphide Sr Pt 3 P. *Physical Review Letters* **2012**, *108*, 237001–237001.
22) Gäbler, F. (Sr3N) E and (Ba3N) E (E= Sb, Bi): Synthesis, crystal structures, and physical properties. *Zeitschrift für anorganische und allgemeine Chemie* **2004**, *630*, 2292–2298.
23) Deng, Z.; Ni, D.; Chen, D.; Bian, Y.; Li, S.; Wang, Z.; Zhao, Y. <scp>Anti-perovskite</scp> materials for energy storage batteries. *InfoMat* **2022**, *4* (2), 12252–12252.

24) Lu, Z.; Ciucci, F. Anti-perovskite cathodes for lithium batteries. *Journal of Materials Chemistry A* **2018**, *6* (12), 5185–5192.
25) Shein, I. R.; Shein, K. I.; Ivanovskii, A. L. Elastic and electronic properties and stability of SrThO3, SrZrO3 and ThO2 from first principles. *Journal of Nuclear Materials* **2007**, *361* (1), 69–77.
26) Nakamura, Y.; Takenaka, K.; Kishimoto, A.; Takagi, H. Mechanical Properties of Metallic Perovskite Mn3Cu0.5Ge0.5N:High-Stiffness Isotropic Negative Thermal Expansion Material. *Journal of the American Ceramic Society* **2009**, *92* (12), 2999–3003.
27) Sun, Y.; Wang, C.; Huang, Q.; Guo, Y.; Chu, L.; Arai, M.; Yamaura, K. Neutron Diffraction Study of Unusual Phase Separation in the Antiperovskite Nitride Mn3ZnN. *Inorganic Chemistry* **2012**, *51* (13), 7232–7236.
28) Zheng, J.; Perry, B.; Wu, Y. Antiperovskite Superionic Conductors: A Critical Review. *ACS Materials Au* **2021**, *1* (2), 92–106.
29) Chern, M. Y.; Disalvo, F. J.; Parise, J. B.; Goldstone, J. A. The structural distortion of the anti-perovskite nitride Ca3AsN. *Journal of Solid State Chemistry* **1992**, *96* (2), 426–435.
30) Tong, P.; Wang, B.-S.; Sun, Y.-P. Mn-based antiperovskite functional materials: Review of research. *Chinese Physics B* **2013**, *22* (6), 067501–067501.
31) He, T.; Huang, Q.; Ramirez, A. P.; Wang, Y.; Regan, K. A.; Rogado, N.; Hayward, M. A.; Haas, M. K.; Slusky, J. S.; Inumara, K.; Zandbergen, H. W.; Ong, N. P.; Cava, R. J. Superconductivity in the non-oxide perovskite MgCNi3. *Nature* **2001**, *411* (6833), 54–56.
32) Okoye, C. Optical properties of the antiperovskite superconductor MgCNi3. *Journal of Physics: Condensed Matter* **2003**, *15* (6), 833–841.
33) Schnell, J.; Günther, T.; Knoche, T.; Vieider, C.; Köhler, L.; Just, A.; Keller, M.; Passerini, S.; Reinhart, G. All-solid-state lithium-ion and lithium metal batteries – paving the way to large-scale production. *Journal of Power Sources* **2018**, *382*, 160–175.
34) Grimvall, G. In *Thermophysical properties of materials*; and others„ Ed.; Elsevier, 1999.
35) Bannikov, V.; Shein, I.; Ivanovskii, A. Elastic properties of anti-perovskite-type Ni-rich nitrides MNNi3 (M= Zn. *Physica B: Condensed Matter* **2010**, (22), 4615–4619.
36) Bang, J.; Park, J.; Lee, K.; Kim, M.; Kyung, W.; Denlinger, J. D.; Kim, Y.; Lee, Y. H.; Kim, C.; Kim, S. W. Antiperovskite Gd3 SnC: Unusual Coexistence of Ferromagnetism and Heavy Fermions in Gd Lattice. *Advanced Materials* **2021**, *33* (37), 2102958–2102958.
37) Wang, Y.; Wang, Q.; Liu, Z.; Zhou, Z.; Li, S.; Zhu, J.; Zou, R.; Wang, Y.; Lin, J.; Zhao, Y. Structural manipulation approaches towards enhanced sodium ionic conductivity in Na-rich antiperovskites. *Journal of Power Sources* **2015**, *293*, 735–740.
38) Zhao, Y.; Daemen, L. L. Superionic Conductivity in Lithium-Rich Anti-Perovskites. *Journal of the American Chemical Society* **2012**, *134* (36), 15042–15047.
39) Aimi, T.; Imada, M. Does Simple Two-Dimensional Hubbard Model Account for High-Tc Superconductivity in Copper Oxides? *Journal of the Physical Society of Japan* **2007**, *76* (11), 113708–113708.
40) Iikubo, S. Local lattice distortion in the giant negative thermal expansion material Mn 3 Cu 1− x Ge x N. *Physical review letters* **2008**, *101*, 205901–205901.
41) Chern, M. Y.; Vennos, D. A.; Disalvo, F. J. Synthesis, structure, and properties of antiperovskite nitrides Ca3MN, M=P, As, Sb, Bi, Ge, Sn, and Pb. *Journal of Solid State Chemistry* **1992**, *96* (2), 415–425.
42) Iqbal, S.; Murtaza, G.; Khenata, R.; Mahmood, A.; Yar, A.; Muzammil, M.; Khan, M. Electronic and Optical Properties of Ca3MN (M = Ge, Sn, Pb, P, As, Sb and Bi) Antiperovskite Compounds. *Journal of Electronic Materials* **2016**, *45* (8), 4188–4196.
43) Beznosikov, B. Predicted Nitrides with an Antiperovskite Structure. *Journal of Structural Chemistry* **2003**, *44* (5), 885–888.
44) Wang, B. S.; Tong, P.; Sun, Y. P.; Li, L. J.; Tang, W.; Lu, W. J.; Zhu, X. B.; Yang, Z. R.; Song, W. H. Enhanced giant magnetoresistance in Ni-doped antipervoskite compounds GaCMn3−xNix(x=0.05,0.10). *Applied Physics Letters* **2009**, *95* (22), 222509–222509.
45) Wang, Y.; Zhang, H.; Zhu, J.; Lü, X.; Li, S.; Zou, R.; Zhao, Y. Antiperovskites with Exceptional Functionalities. *Advanced Materials* **2020**, *32* (7), 1905007–1905007.
46) Kanchana, V. .; C, N. X. Mechanical properties of Ti3AlX. *Europhysics Letters)* **2009**, *87* (2), 26006–26006.
47) Bilal, M.; Jalali-Asadabadi, S.; Ahmad, R.; Ahmad, I. Electronic Properties of Antiperovskite Materials from State-of-the-Art Density Functional Theory. *Journal of Chemistry* **2015**, *2015*, 1–11.
48) Ullah, I.; Murtaza, G.; Khenata, R.; Mahmood, A.; Muzzamil, M.; Amin, N.; Saleh, M. Structural and Optoelectronic Properties of X3ZN (X = Ca, Sr, Ba; Z = As, Sb, Bi) Anti-Perovskite Compounds. *Journal of Electronic Materials* **2016**, *45* (6), 3059–3068.
49) Krivovichev, S. V. Minerals with antiperovskite structure: a review. *Zeitschrift für Kristallographie-Crystalline Materials* **2008**, *223*, 109–113.
50) Lai, K. T.; Antonyshyn, I.; Prots, Y.; Valldor, M. Anti-Perovskite Li-Battery Cathode Materials. *Journal of the American Chemical Society* **2017**, *139* (28), 9645–9649.
51) Howard, J.; Hood, Z. D.; Holzwarth, N. Fundamental aspects of the structural and electrolyte properties of Li 2 OHCl from simulations and experiment. *Physical Review Materials, 2017 1* (7), 75406–75406.
52) Deng, Z.; Ou, M.; Wan, J.; Li, S.; Li, Y.; Zhang, Y.; Deng, Z.; Xu, J.; Qiu, Y.; Liu, Y.; Fang, C.; Li, Q.; Huang, L.; Zhu, J.; Han, S.; Han, J.; Zhao, Y. Local Structural Changes and Inductive Effects on Ion Conduction in Antiperovskite Solid Electrolytes. *Chemistry of Materials* **2020**, *32* (20), 8827–8835.
53) Qi, Y.; Hector, L. G.; James, C.; Kim, K. J. Lithium Concentration Dependent Elastic Properties of Battery Electrode Materials from First Principles Calculations. *Journal of The Electrochemical Society* **2014**, *161* (11), F3010–F3018.
54) Oudah, M.; Ikeda, A.; Hausmann, J. N.; Yonezawa, S.; Fukumoto, T.; Kobayashi, S.; Sato, M.; Maeno, Y. Superconductivity in the antiperovskite Dirac-metal oxide Sr3−xSnO. *Nature Communications* **2016**, *7* (1), 1–6.
55) Fox, M. Optical properties of solids. *American Journal of Physics* **2002**, *70* (12), 1269.
56) Haddadi, K.; Bouhemadou, A.; Louail, L.; Maabed, S.; Maouche, D. Structural and elastic properties under pressure effect of the cubic antiperovskite compounds ANCa3 (A=P, As, Sb, and Bi). *Physics Letters A* **2009**, *373* (20), 1777–1781.
57) Bouhemadou, A.; Zerarga, F.; Almuhayya, A.; Bin-Omran, S. FP-LAPW study of the fundamental properties of the cubic spinel CdAl2O4. *Materials Research Bulletin* **2011**, *46* (12), 2252–2260.
58) Cox, D.; Sleight, A. Mixed-valent Ba2Bi3+ Bi5+ O6: structure and properties vs temperature. *Acta Crystallographica Section B: Structural Crystallography and Crystal Chemistry* **1979**, *35* (1), 1–10.
59) Pena, M. A.; Fierro, J. L. G. ChemInform Abstract: Chemical Structures and Performance of Perovskite Oxides. *ChemInform* **2001**, *32* (39), no–no.
60) Manthiram, A.; Yu, X.; Wang, S. Lithium battery chemistries enabled by solid-state electrolytes. *Nature Reviews Materials* **2017**, *2* (4), 16103–16103.
61) Dawson, J. A.; Canepa, P.; Famprikis, T.; Masquelier, C.; Islam, M. S. Atomic-Scale Influence of Grain Boundaries on Li-Ion Conduction in Solid Electrolytes for All-Solid-State Batteries. *Journal of the American Chemical Society* **2018**, *140* (1), 362–368.
62) Zachary, D. H.; Hui, W.; Amaresh, S. P. Li2OHCl Crystalline Electrolyte for Stable Metallic Lithium Anodes. *J. Am. Chem. Soc* **2016**, *138*, 1768–1771.
63) Kamishima, K. Giant magnetoresistance in the intermetallic compound Mn 3 GaC. *Physical Review B* **2000**, *63* (2), 24426–24426.
64) De Graef, M.; Mchenry, M. E. In *Structure of materials: an introduction to crystallography, diffraction and symmetry*; and others„ Ed.; Cambridge University Press, 2012.
65) Wang, B. Large magnetic entropy change near room temperature in anti-perovskite SnCMn3. *Europhysics Letters* **2009**, *85* (4), 47004–47004.
66) Jingfeng, Z.; Brian, P.; Wu, Y. Anti-perovskite Superionic Conductors: A Critical Review. *ACS Mater. Au* **2021**, *1*, 92–106.

67) Yu, M.-H.; Lewis, L. H.; Moodenbaugh, A. R. Large magnetic entropy change in the metallic antiperovskite Mn3GaC. *Journal of Applied Physics* **2003**, *93* (12), 10128–10130.
68) Bauer, E. Heavy fermion superconductivity and magnetic order in noncentrosymmetric C e P t 3 S i. *Physical review letters* **2004**, *92*, 27003–27003.
69) Wang, R.; Zhang, X.; He, J.; Bu, K.; Zheng, C.; Lin, J.; Huang, F. Synthesis, Structure, and Optical Properties of Antiperovskite-Derived Ba2MQ3X (M = As, Sb; Q = S, Se; X = Cl, Br, I) Chalcohalides. *Inorganic Chemistry* **2018**, *57* (3), 1449–1454.
70) Nandkishore, R.; Maciejko, J.; Huse, D. A.; Sondhi, S. L. Superconductivity of disordered Dirac fermions. *Physical Review B* **2013**, *87* (17), 174511–174511.
71) Schwering, G.; Hönnerscheid, A.; van Wüllen Priv.-Doz, L.; Jansen, M. High Lithium Ionic Conductivity in the Lithium Halide Hydrates Li3-n (OHn) Cl ($0.83 \leq n \leq 2$) and Li3-n (OHn) Br ($1 \leq n \leq 2$) at Ambient Temperatures. *ChemPhysChem* **2003**, *4* (4), 343–348.
72) Hartwig, P.; Rabenau, A.; Weppner, W. Lithium hydroxide halides: phase equilibria and ionic conductivities. *Journal of the Less Common Metals* **1981**, *78* (2), 227–233.
73) Kwangnam, K.; S, D. J. Predicting Wettability and the Electrochemical Window of Lithium-Metal/Solid Electrolyte Interfaces. *ACS Applied Materials & Interfaces* **2019**, *11*, 39940–39950.
74) Yiran, X.; Kostiantyn, T.; Aashray, N. Electrolyte melt infiltration for scalable manufacturing of inorganic all-solid-state lithium-ion batteries. *Nature Materials* **2021**, *20*, 984–990.